Investigating the origin of dielectric responses in semiconductor devices using equilibrium photocapacitance measurements

Muhammed Raees A., Greeshma L. S., Anjana K. N., and Manoj A. G. Namboothiry*
School of Physics, Indian Institute of Science Education and Research Thiruvananthapuram, Maruthamala (P.O.), Vithura, Thiruvananthapuram, Kerala 695551, India

(Received 7 June 2024; revised 11 November 2025; accepted 26 November 2025; published 22 December 2025)

A new dielectric spectroscopic technique, termed equilibrium photocapacitance measurement (EPCM), using the Lorentz oscillator model, has been developed to understand the photocapacitance of semiconductor devices. This new technique reveals that the density of dipoles and the dipole moment of each dipole in a semiconductor change under illumination. These changes counteract and lead to an equilibrium at a specific applied AC frequency ω_e, at which the photocapacitance response (PCR), a frequency-dependent phenomenon, vanishes. The measured ω_e is found to be equivalent to a fundamental parameter governing charge dynamics, the effective Lorentz resonant frequency (ω_0), that cannot be measured directly. Here, we use EPCM to probe ω_0 indirectly via measuring ω_e to investigate how external perturbations (light, DC bias, etc.) influence the dielectric properties of a semiconductor device. Using ITO/PTB7/Ag and ITO/ZnO/PTB7/MoO_3/Ag devices, we demonstrate that EPCM allows probing both free and bound charge carriers, unlike conventional current measurements, which only account for the mobile charges. Additionally, EPCM enables precise identification of bound and free charge dominated regimes in the C-V profile and provides a robust method to determine the intrinsic dielectric constant of materials, which is challenging to ascertain due to its sensitivity to measurement conditions.

DOI: 10.1103/y879-hx9f

I. INTRODUCTION

Capacitance measurement is a versatile tool for investigating and improving the electrical properties of semiconductor materials. The capacitance of a semiconductor device depends on the distribution of charge carriers (electrons and holes) inside the material [1,2]. This charge distribution inside a device under test (DUT) changes under external perturbations like DC bias, illumination, etc., leading to a capacitance response, which is a signature of the electrical properties of the DUT [3]. Capacitance measurements are widely used by researchers all over the world for various purposes, including doping profile characterization in semiconductors [4–7], quality assessment of insulating layers in devices like MOS capacitors [8], extraction of key parameters such as carrier concentration [6,9–11], threshold voltage, and interface states [12–15] in semiconductor devices, monitoring the fabrication processes to ensure the desired electrical characteristics of semiconductor devices [16], etc. In the context of optoelectronic devices, the C-V measurements are useful for investigating the interface states [17], evaluating junction quality [18], determining trap states [19–21], optimizing passivation layers [14,19], etc.

C-V measurement necessitates an analytical model depending on the requirements and specific characteristics of the device being analyzed. Various models, including metal-oxide-semiconductor (MOS) capacitance model [22–26], high-frequency C-V model [27–29], surface potential model [16,30–33], charge control model [34–36], quasistatic C-V model [37–41], small-signal models [42–45], charge-based capacitance models [46–49], etc., have been employed to analyze the C-V response of devices, especially for understanding the carrier transport. These models are often implemented using simulation tools for device characterization, design, and optimization. However, all these models are macroscopic models capable of interpreting the overall performance of the DUT, and it is difficult to analyze the DUT microscopically. Hence, investigating the charge carrier transport, trapping, photo-generation, recombination, etc., is difficult using these models. Also, several models interpret capacitance solely on charge accumulation, which is a DC capacitance perspective. This can be different from the AC capacitance measured by LCR meters, which arises from charge oscillations rather than a buildup of charge. This paper introduces a more comprehensive microscopic picture of dielectric response using the Lorentz oscillator model that considers the effects of both charge accumulation and oscillations.

The Lorentz oscillator model is a promising model which has the potential to comprehend the electrical properties of materials and the charge carrier dynamics in devices. In the context of semiconducting materials, the Lorentz oscillator model is widely used in optical spectroscopy [50–52], nanophotonics [53,54], plasmonics [55–57], ellipsometry [11,58–60], etc. However, this model has not been explored yet for understanding the charge carrier dynamics in semiconductor devices using electrical characterization. This model is a theoretical framework giving the microscopic description of dielectric characteristics of semiconductors, insulators, and metals [61,62]. The dielectric function describes how a material responds to an applied electric field and is essential for

*Contact author: manoj@iisertvm.ac.in

comprehending optical and electrical properties. According to the Lorentz oscillator model, electrons in a semiconductor can be considered as simple harmonic oscillators and they oscillate when an external oscillating electric field is introduced. Lorentz quantified the dielectric response (ϵ_r) of a material arising from this oscillatory motion of electrons as a function of the frequency (ω) of the oscillating external field [61,62]. Usually, ϵ_r is measured over a wide range of ω and the data is fitted with Lorentz dielectric function to extract the fitting parameters plasma frequency (ω_p), resonant frequency (ω_0), background dielectric constant (ϵ_∞), and damping factor (γ) [50,57]. There may be multiple resonant frequencies and damping factors in some systems. Fitting a single set of data with more than three fitting parameters without any prior information about the system will not guarantee the meaningfulness of the extracted fitting parameters. Also, Lorentz explained the variation of ϵ_r with ω and this picture can't be used as such for modeling or interpreting the effects of DC bias and illumination on the capacitance of semiconductor devices.

This work is an investigation of how the photogeneration and injection of charges alter the dielectric properties of a semiconductor. A novel technique called equilibrium photocapacitance measurement (EPCM) is introduced in this work to investigate the changes in ω_0 with DC bias and illumination using an equivalent parameter named equilibrium frequency (ω_e).

II. THEORY

A. Effect of illumination on the Lorentz model

To derive the total change in capacitance under illumination, consider the general expression for dielectric constant, i.e.,

$$\epsilon_r(\omega) = \epsilon_\infty + \frac{N}{\epsilon_0} \times RP\left(\frac{\tilde{p}(\omega)}{\tilde{E}(\omega)}\right), \tag{1}$$

where $\tilde{p}(\omega)$ is the time-varying dipole moment of the oscillating dipole due to the oscillating electric field $\tilde{E}(\omega)$. The fraction $\frac{\tilde{p}(\omega)}{\tilde{E}(\omega)}$ is complex and its real part (or the real part of the dielectric function) leads to the the capacitance (see Sec. S2 in the Supplemental Material for more details) [63]. From the Lorentz oscillator model [61,62],

$$RP\left(\frac{\tilde{p}(\omega)}{\tilde{E}(\omega)}\right) = \frac{p}{E} = \frac{e^2}{m} \times \left[\frac{\left(\omega_0^2 - \omega^2\right)}{\left(\omega_0^2 - \omega^2\right)^2 + \omega^2\gamma^2}\right]. \tag{2}$$

Since γ is the damping offered to the oscillation by the medium, it is assumed to be a material constant. Then ω_0 may be the only parameter changing under illumination leading to a change in the dipole moment of each dipole. Therefore, the total change in dielectric constant under illumination can be written as

$$\Delta\epsilon_r(\omega) = \Delta\epsilon_1 + \Delta\epsilon_2 \tag{3}$$

$$\Delta\epsilon_1 = \frac{p\Delta N}{\epsilon_0 E} = \frac{e^2\Delta N}{m\epsilon_0}\left[\frac{\left(\omega_0^2 - \omega^2\right)}{\left(\omega_0^2 - \omega^2\right)^2 + \omega^2\gamma^2}\right] \tag{4}$$

$$\Delta\epsilon_2 = \frac{N}{\epsilon_0} \times \Delta\left(\frac{p}{E}\right)$$

$$= \frac{e^2\Delta\omega_0}{m\epsilon_0}\left[\frac{2N\omega_0}{\left(\omega_0^2 - \omega^2\right)^2 + \omega^2\gamma^2} + \frac{4N\omega_0\left(\omega_0^2 - \omega^2\right)^2}{\left[\left(\omega_0^2 - \omega^2\right)^2 + \omega^2\gamma^2\right]^2}\right], \tag{5}$$

where $\Delta\epsilon_1$ and $\Delta\epsilon_2$ are the contributions to the change in dielectric constant under illumination arising from the changes in the number density of dipoles and dipole moment of each dipole, respectively.

The change in resonant frequency ($\Delta\omega_0$) mentioned in Eq. (5) is a consequence of the photogeneration of charges. In order to correlate $\Delta\omega_0$ to ΔN, assuming a system (or a material) consisting of N_f number of free charges and N_b number of bound charges per unit volume ($N_f + N_b = N$) having resonant frequencies ω_f and ω_b, respectively ($\omega_f < \omega_b$). The effective resonant frequency of the system is the ensemble average given by

$$\omega_0 = \frac{N_f\omega_f + N_b\omega_b}{N_f + N_b} \tag{6}$$

$$\Delta\omega_0 = \left[\frac{\partial\omega_0}{\partial N_f} \times \Delta N_f\right] + \left[\frac{\partial\omega_0}{\partial N_b} \times \Delta N_b\right], \tag{7}$$

where ΔN_f and ΔN_b are the change in densities of free carriers and bound carriers due to illumination ($\Delta N_f + \Delta N_b = \Delta N$). Here, free carriers are those charges which can take part in conduction if there is a potential difference across material and bound carriers are those charges which can never participate in conduction even if there is a potential difference.

B. Modeling light-induced changes to the dielectric properties

From Eqs. (1), (2), the Lorentz dielectric functions under dark and light conditions, and the corresponding photocapacitance response (PCR) can be written as

$$\epsilon_{r,\mathrm{Dark}}(\omega) - \epsilon_\infty = \frac{(N_f + N_b)e^2\left[\omega_{0,\mathrm{Dark}}^2 - \omega^2\right]}{m\epsilon_0\left[\left(\omega_{0,\mathrm{Dark}}^2 - \omega^2\right)^2 + \omega^2\gamma^2\right]} \tag{8}$$

$$\epsilon_{r,\mathrm{Light}}(\omega) - \epsilon_\infty = \frac{(N_f + N_b + \Delta N)e^2\left[\omega_{0,\mathrm{Light}}^2 - \omega^2\right]}{m\epsilon_0\left[\left(\omega_{0,\mathrm{Light}}^2 - \omega^2\right)^2 + \omega^2\gamma^2\right]} \tag{9}$$

$$\Delta\epsilon_r(\omega) = \epsilon_{r,\mathrm{Light}}(\omega) - \epsilon_{r,\mathrm{Dark}}(\omega) \tag{10}$$

$$\omega_{0,\mathrm{Dark}} = \frac{N_f\omega_f + N_b\omega_b}{N_f + N_b} \tag{11}$$

$$\omega_{0,\mathrm{Light}} = \frac{(N_f + \Delta N_f)\omega_f + (N_b + \Delta N_b)\omega_b}{N_f + N_b + \Delta N}, \tag{12}$$

where $\omega_{0,\mathrm{Dark}}$ and $\omega_{0,\mathrm{Light}}$ are the average resonant frequency of the system under dark and light conditions, respectively and $\Delta\epsilon_r$ (which is equivalent to ΔC) represent the PCR.

III. RESULTS AND DISCUSSION

A metal-semiconductor-metal (M-S-M) structure with an organic material as the semiconductor is used to investigate

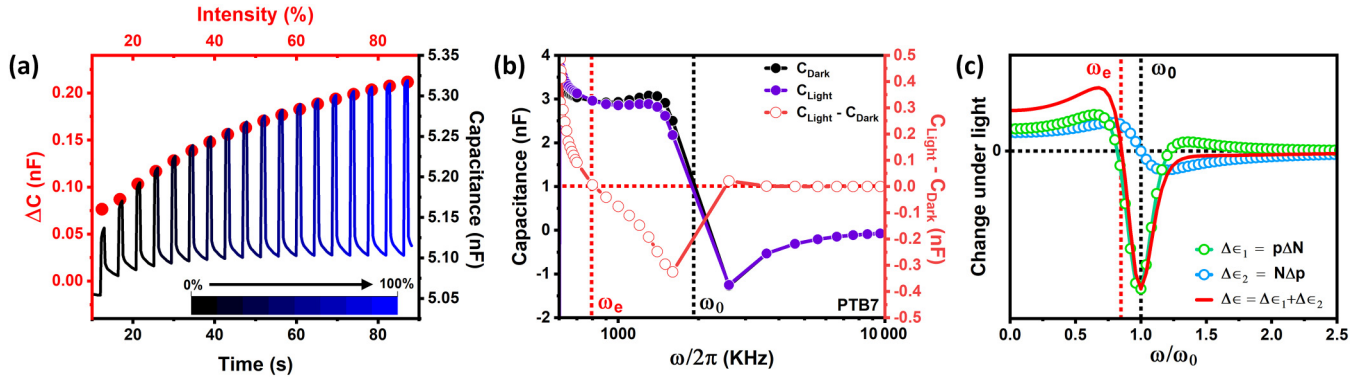

FIG. 1. (a) Photo-capacitance response of ITO/PTB7/Ag device under light perturbation with increasing intensity (blue/black) and the corresponding change in capacitance (red), (b) the capacitance-frequency response of ITO/PTB7/Ag device measured under dark and light conditions and (c) the simulation representing the different contributions to the change in the dielectric constant of a material due to light perturbation.

the effects of illumination and DC bias on capacitance measurement. A device with structure ITO/PTB7/Ag [Fig. S10(a)] is fabricated for this purpose by following the procedure mentioned in the experimental methods (see Sec. S1(I) in the Supplemental Material) [63,66,67]. To address the dielectric properties of the material, the capacitance of the fabricated device is measured using an LCR meter by applying an AC voltage of a definite frequency (ω) [68]. The microscopic picture of the measured capacitance can be deduced from the Lorentz oscillator model as (see Sec. S2 in the Supplemental Material for more details) [61–63,69–71]

$$C(\omega) = \frac{\epsilon_0 A}{d} \times \epsilon_r(\omega) = \frac{\epsilon_0 A}{d}\left[\epsilon_\infty + \left(\frac{Ne^2}{m\epsilon_0} \times \frac{\left(\omega_0^2 - \omega^2\right)}{\left(\omega_0^2 - \omega^2\right)^2 + \omega^2\gamma^2}\right)\right], \tag{13}$$

where ϵ_0 is the permittivity of free space, A is the area of the device, d is the thickness of the semiconductor layer, ϵ_r is the dielectric constant, ϵ_∞ is the background dielectric constant, N is the number of electrons per unit volume, e is the electronic charge, m is the mass of an electron, ω_0 is the resonant frequency, ω is the frequency of the applied oscillating field, and γ is the damping factor of the material.

A. Effect of illumination on dielectric properties

The capacitance of the device is found to be changing under illumination with $\lambda \sim 530$ nm [Fig. 1(a)] and this change can be attributed to the change in carrier concentration ($N \rightarrow N + \Delta N$) [72,73]. A detailed discussion on the origin of this photo response is provided in the Supplemental Material (Sec. S4) [63,74–79]. It is confirmed that the incident wavelength doesn't have any role other than the photogeneration and there is no need for the collection of these photogenerated carriers from active material to the electrodes to observe this photoresponse (Fig. S11) [63]. If N is the only parameter in Eq. (13) that changes under illumination, then the change in capacitance of the device due to light, the photo-capacitance response (PCR), can be expressed as

$$\Delta C = C_{\text{Light}} - C_{\text{Dark}} = \frac{Ae^2}{md} \times \left[\frac{\left(\omega_0^2 - \omega^2\right)}{\left(\omega_0^2 - \omega^2\right)^2 + \omega^2\gamma^2}\right] \times \Delta N. \tag{14}$$

A light intensity-dependent measurement is performed on ITO/PTB7/Ag device at constant ω and ΔC is found to be increasing sublinearly with intensity as shown in Fig. 1(a). This confirms that the photogeneration of carriers is the origin of PCR but ΔC and ΔN are not linearly proportional as described in Eq. (14). It is possible only if the coefficient of ΔN in Eq. (14) decreases with intensity. Also, the measured ΔC is a function of ω according to Eq. (14) and it should be zero at $\omega = \omega_0$ (resonance). The capacitance-frequency (C-F) measurement is done on ITO/PTB7/Ag device under dark and light conditions and ΔC is calculated as shown in Fig. 1(b). It is observed that ΔC vanishes at a frequency less than ω_0. Hence, it can be concluded that N is not the only parameter in Eq. (13) that changes under illumination. Since γ is the resistance offered to the oscillations of the charges by the medium, it is assumed to be a material constant. Then ω_0 may be the second parameter in Eq. (13) that changes under illumination leading to a change in the dipole moment of each dipole. Therefore, the total change in dielectric constant under illumination is given by Eq. (3), i.e., the change in dielectric constant under illumination is arising from the changes in the number density of dipoles ($\Delta\epsilon_1$) and dipole moment of each dipole ($\Delta\epsilon_2$), respectively. At a particular frequency, these contributions counteract and cancel each other, giving zero photoresponse (i.e., $\Delta\epsilon_r = \Delta C = 0$) as shown in Fig. 1(c). This particular frequency is named the equilibrium frequency (ω_e), and the capacitance measured at this frequency is named the equilibrium capacitance (C_e).

The effective resonant frequency (ω_0) of the system can be considered as the average value of the resonance frequencies of free and bound carriers (ω_f and ω_b) as shown in Eq. (6), and its change under illumination is given in Eq. (7). Here, free carriers are those charges which can take part in conduction if there is a potential difference across the material, and bound carriers are those charges which can never

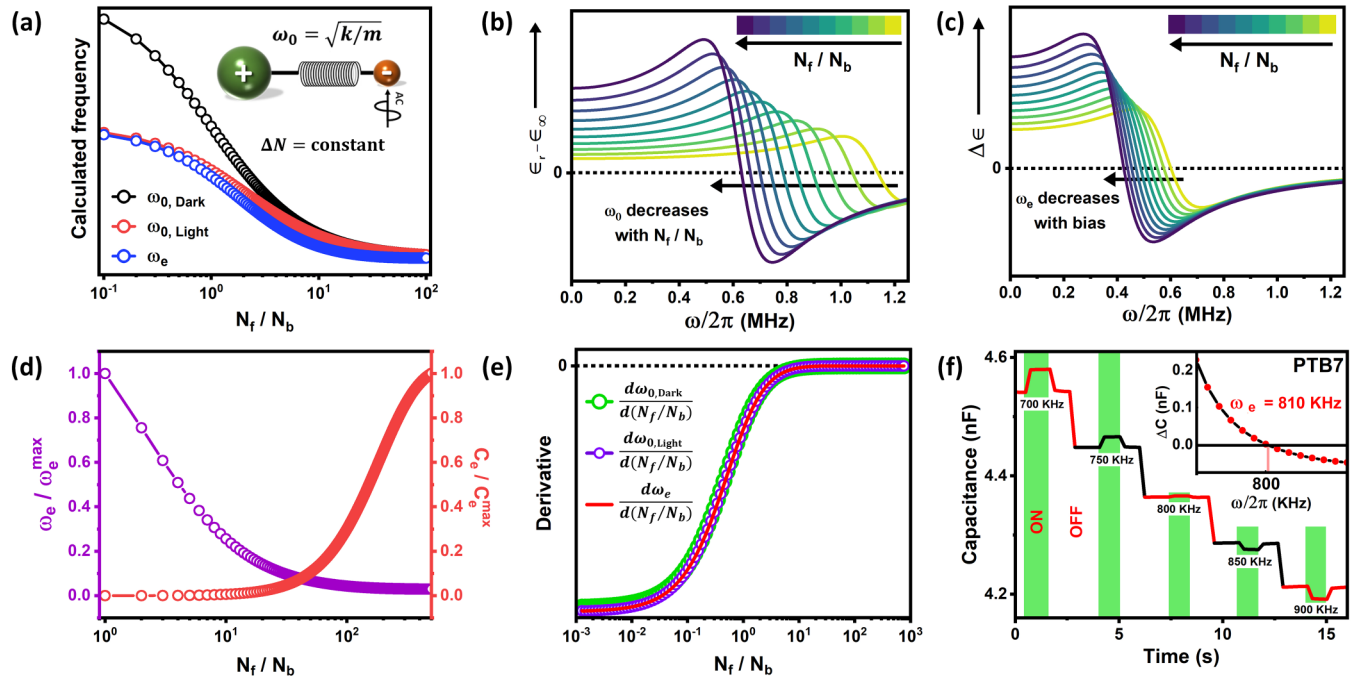

FIG. 2. (a) The simulated trends of $\omega_{0,\text{Dark}}$, $\omega_{0,\text{Light}}$ and ω_e with the ratio N_f/N_b, (b) the change in Lorentz dielectric function with N_f/N_b, (c) change in PCR ($\Delta C \equiv \Delta\epsilon_r$) with N_f/N_b, (d) the normalized changes in equilibrium frequency (ω_e) and equilibrium capacitance (C_e), (e) the derivatives of $\omega_{0,\text{Dark}}$, $\omega_{0,\text{Light}}$ and ω_e with respect to (N_f/N_b) at different (N_f/N_b) and (f) the change in capacitance under light perturbation measured at different AC frequencies and the inset shows $\Delta C = C_{\text{Light}} - C_{\text{Dark}}$ at different frequencies measured for ITO/PTB7/Ag device.

participate in conduction even if there is a potential difference. The bound charges include the charges whose motion is restricted by the trap states inside the material or interfaces between different layers of a device (for instance the interface between the electron transport layer or hole transport layer and active material in thin film solar cells), etc. These charges having constraints to their motion form a space charge region in the active material and they have resonant frequencies (ω_b) in the range $10^3 - 10^6$ Hz [80]. On the other hand, free carriers do not experience any restrictions to their motion and their resonance frequency (ω_f) is ideally zero, but experimentally it can be obtained as a value close to zero due to experimental limitations. If both types of charges are present in the system, the degree of boundedness of the charges can be represented by the superposition represented by Eq. (6). Therefore, the ratio of free carriers to the bound carriers (N_f/N_b) inside the material is different under dark and light conditions leading to two different resonant frequencies $\omega_{0,\text{Dark}}$ and $\omega_{0,\text{Light}}$, respectively [Fig. 2(a)].

The effect of N_f/N_b on the Lorentz dielectric function, PCR, ω_e and C_e are shown in Figs. 2(b), 2(c), 2(d). Hence, one can probe the variation in N_f/N_b under different conditions of illumination or DC bias by probing ω_0 using photocapacitance measurement meanwhile the conventional current measurements will give information about the dynamics of free charges only. However, it is difficult to probe ω_0 using electrical measurements. To overcome this difficulty, the equilibrium frequency (ω_e) can be probed instead of the resonant frequency (ω_0). The simulation result shows that the derivatives of $\omega_{0,\text{Dark}}$, $\omega_{0,\text{Light}}$ and ω_e with respect to (N_f/N_b) are equal at all conditions [Fig. 2(e)]. Hence, the change in ω_0 will be reflected as such in ω_e. Hence, a new experiment, named equilibrium photo-capacitance measurement (EPCM), is designed to systematically measure ω_e and C_e of an M-S-M device [Fig. 2(f)] under different conditions of illumination and DC bias (details are given in Sec. S1 of the Supplemental Material) [63].

The simulation results shows that the Lorentz dielectric function and PCR shift towards low frequency region with increase in illumination intensity as shown in Figs. 3(a), 3(b). During the simulation $\omega_{0,\text{Dark}}$ is kept constant because N_f/N_b under dark is remaining a constant. But N_f increases with increase in illumination intensity and hence the resonant frequency reduces under illumination ($\omega_{0,\text{Light}} < \omega_{0,\text{Dark}}$). This reduction is negligible when $N_f \gg N_b$ and dominant otherwise [Fig. 2(a)]. The variation in $\omega_{0,\text{Light}}$ and ω_e with illumination intensity are calculated from the simulated curves and are shown in Fig. 3(c). When the intensity increases, ω_e follows the trend of $\omega_{0,\text{Light}}$. At significantly higher intensities $\omega_e \approx \omega_{0,\text{Light}}$ and it saturates to a value ω_f at very high intensities. The simulated variation of ω_e is consistent with the experimental observation [Fig. 3(d)]. Also, the sublinear behavior of PCR (measured at 10 KHz) with illumination intensity is also simulated as shown in Fig. 3(e), which confirms the validity of the proposed theory.

B. Effect of DC bias on dielectric properties

To explore the effect of DC bias on the Lorentz dielectric function, EPCM is performed on ITO/PTB7/Ag device under different DC bias conditions and the measured ω_e and C_e are shown in Fig. 4(a). At 0 V, ω_e is maximum and decreases with forward and reverse voltages. From the current-voltage (I-V) and capacitance-voltage (C-V) measurements of the device,

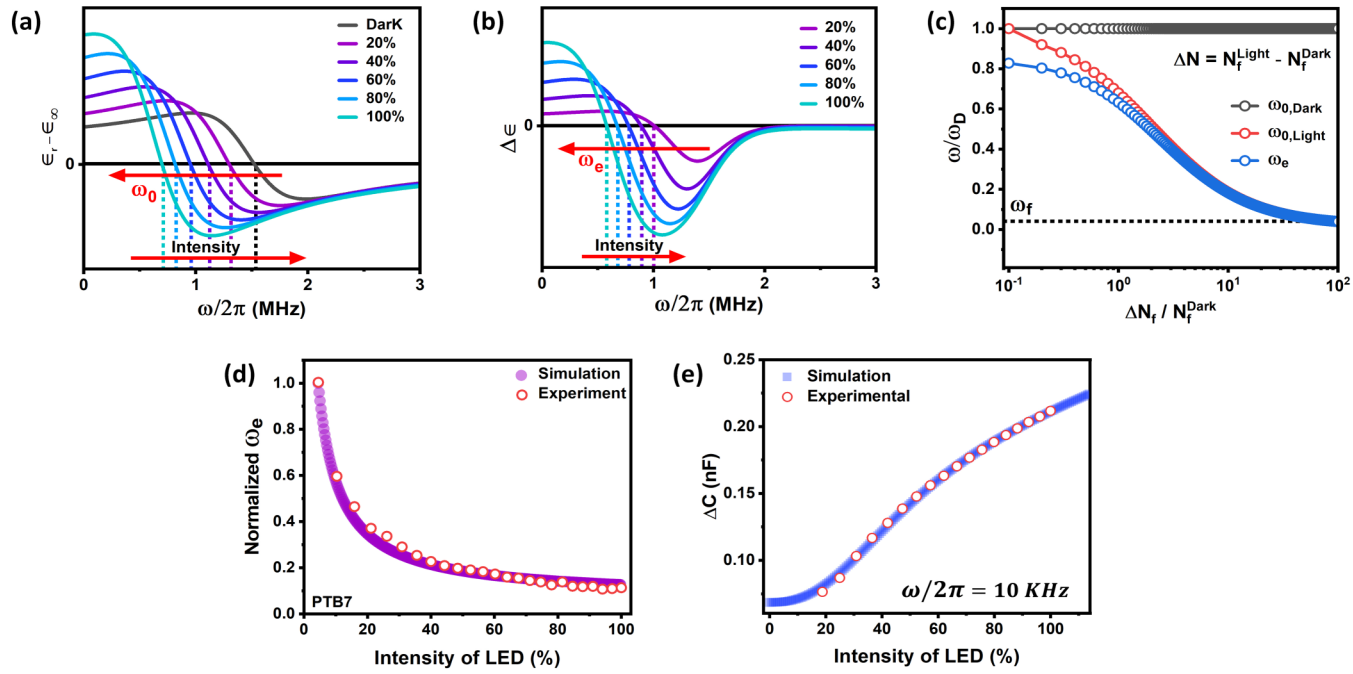

FIG. 3. (a) The simulated change in Lorentz dielectric function with the intensity of illumination, (b) the corresponding PCR at different intensities (experimental results are shown in Fig. S4) and (c) the change in $\omega_{0,\mathrm{Dark}}$, $\omega_{0,\mathrm{Light}}$ and ω_e with intensities. (d) and (e) shows the simulated and experimental changes in ω_e and ΔC (at a constant frequency) with illumination intensity respectively for ITO/PTB7/Ag device.

it is confirmed that the device has a symmetric M-S-M architecture and hence the current increases with positive and negative voltages (Fig. S10) [63]. According to the previous discussion, those charges that can take part in conduction are counted as free charges. Hence, it can be considered that N_f increases with positive and negative voltages, resulting

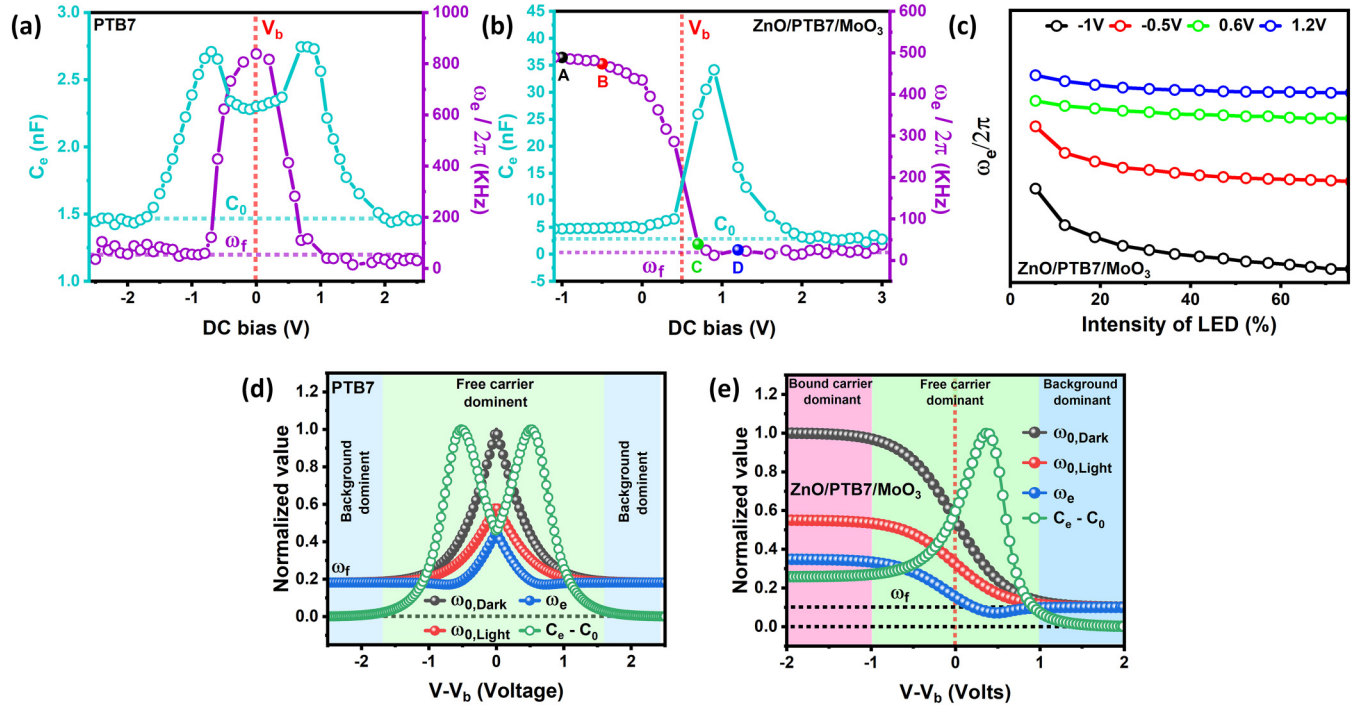

FIG. 4. (a) The variation in C_e and ω_e of ITO/PTB7/Ag device with DC bias, (b) the variation in C_e and ω_e of ITO/ZnO/PTB7/MoO_3/Ag device with DC bias [the built-in voltage calculation from C-V is shown in Figs. S10(a,b)], (c) the change in ω_e of ITO/ZnO/PTB7/MoO_3/Ag device with intensity measured at four different DC bias conditions [labeled as A, B, C, and D in Fig. 4(c)], (d) the simulated changes in $\omega_{0,\mathrm{Dark}}$, $\omega_{0,\mathrm{Light}}$, ω_e, and C_e with DC bias for ITO/PTB7/Ag device and (e) the simulated changes in $\omega_{0,\mathrm{Dark}}$, $\omega_{0,\mathrm{Light}}$, ω_e, and C_e with DC bias for ITO/ZnO/PTB7/MoO_3/Ag device.

in the reduction of $\omega_{0,\mathrm{Dark}}$ [Eq. (11)] and consequently ω_e decreases and saturates at higher DC bias during EPCM. To confirm the reduction of ω_e (or $\omega_{0,\mathrm{Dark}}$) with an increase in charge flow, another device is fabricated with structure ITO/ZnO/PTB7/MoO_3/Ag (band diagram is shown in Fig. S10) [63]. Here, ZnO and MoO_3 act as the electron transport layer (ETL) and (hole transport layer (HTL), respectively. This structure is chosen because it has more control over the charge injection, i.e., charge injection is minimal under reverse bias and increases with forward bias. Under reverse bias condition (ITO is positive and Ag is negative), ZnO and MoO_3 act as the hole blocking layer and electron blocking layer, respectively. Hence, the charge flow is restricted by the interface, and only a very few charges flow through the interfaces. So, most of the charges in PTB7 are bounded under reverse bias condition (i.e., $N_f << N_b$) leading to a higher saturation value of ω_e as shown in Fig. 4(b). Under forward bias condition (ITO is negative and Ag is positive) ZnO and MoO_3 act as the electron transport layer and hole transport layer, respectively, and promote the carrier injection resulting in a high current. Consequently, ω_e decreases under forward bias and reaches a saturation value ω_f as shown in Fig. 4(b). This saturation value of ω_e means that, most of the carriers are in the free state above +0.6V.

For further confirmation, an intensity-dependent EPCM is performed on the ITO/ZnO/PTB7/MoO_3/Ag device under four different DC bias conditions labeled A, B, C and D (−1V, −0.5V, 0.6V, 1.2V, respectively) in Fig. 4(b), and the results are shown in Fig. 4(c). When the reverse bias voltage is increased from −0.5V to −1V (B → A) charge injection or transport does not increase because of the ZnO and MoO_3 layers, resulting in similar ω_e value at both B and A. But the density of free carriers and photocurrent increases with an increase in illumination intensity and results in a reduction of ω_e at A and B. The points C and D represent the forward bias condition. The majority of the charges inside the material are free at C ($N_f \gg N_b$) and hence $\omega_{0,\mathrm{Dark}} \approx \omega_f$ [Eq. (11)]. At this condition, the illumination also introduces photogenerated free carriers to the system and results in $\omega_{0,\mathrm{Light}} \approx \omega_f$ [Eq. (12)]. If the resonant frequencies under dark and light are same, then PCR can be calculated from Eq. (10) as

$$\Delta\epsilon_r(\omega) = \frac{e^2}{m\epsilon_0} \times \frac{\left(\omega_f^2 - \omega^2\right)}{\left(\omega_f^2 - \omega^2\right)^2 + \omega^2\gamma^2} \times \Delta N. \tag{15}$$

The equilibrium frequency and the equilibrium capacitance (at which $\Delta\epsilon_r(\omega) = 0$) at high carrier injection condition can be obtained from Eqs. (13), (15) as

$$\omega_e \approx \omega_f \tag{16}$$

$$C_e = C_0 = \frac{\epsilon_0 A}{d} \times \epsilon_\infty, \tag{17}$$

where C_0 is the capacitance due to the background dielectric constant (ϵ_∞) of the material without any contribution from the charge carriers, generally known as the geometric capacitance. Therefore, ω_e and C_e remains a constant under high carrier injection condition without being affected by the DC bias or illumination intensity as shown in Figs. 4(a), 4(b). This is consistent with the simulation results discussed before [Figs. 2(a) and 3(c)].

In Eq. (13), if $\omega \to \infty$, then the measured dielectric constant $\epsilon_r \to \epsilon_\infty$. Hence, finding the capacitance at the highest possible frequency (usually less than 2 MHz) to find the background dielectric constant is a common practice. However, accuracy may not actually be guaranteed at that frequency. Hence, calculating the background dielectric constant of a material by choosing the appropriate measurement conditions is a challenging task [81] and all those difficulties can be overcome by EPCM technique, i.e., one can calculate ϵ_∞ by measuring C_e at higher forward bias where $C_e \approx C_0$ (where C_0 is the saturation value of C_e vs DC bias). The dielectric constant of PTB7 is calculated to be ∼3.1 [Fig. 4(a)] and is consistent with the previous reports [81,82]. To validate the generality of the experimental observations and the theoretical aspects proposed in the work, the experiments are repeated on ITO/PCBM/Ag device (where PCBM is an acceptor molecule). The results are consistent with that of ITO/PTB7/Ag device, and in good agreement with the proposed theory (Fig. S13) [63].

The simulated trends of $\omega_{0,\mathrm{Dark}}$, $\omega_{0,\mathrm{Light}}$, ω_e, and C_e of both ITO/PTB7/Ag and ITO/ZnO/PTB7/MoO_3/Ag devices are shown in Figs. 4(d), 4(e), respectively. The C_e and ω_e vs DC bias curves have three different regions, i.e., bound carrier dominant, free carrier dominant, and background dominant regions. In the first region, no free electrons are created by the bias and photogeneration only gives the free carriers leading to a saturation value of $\omega_{0,\mathrm{Dark}}$, $\omega_{0,\mathrm{Light}}$, ω_e, and C_e. In the second region, carrier injection leads to an increase in N_f resulting in a reduction in $\omega_{0,\mathrm{Dark}}$, $\omega_{0,\mathrm{Light}}$, and ω_e. The equilibrium capacitance increases first because of the increase in N_f, reaches a maximum, and then decreases due to the decrease in difference between $\omega_{0,\mathrm{Dark}}$ and $\omega_{0,\mathrm{Light}}$. In the third region the carrier injection is dominant and results in a huge number of free charges. Hence, $\omega_{0,\mathrm{Dark}}$ and $\omega_{0,\mathrm{Light}}$ overlaps and the equilibrium frequency will be $\omega_e \approx \omega_f$ [Eq. (16)]. At this condition, the background dielectric constant alone contributes to the equilibrium capacitance, i.e., $C_e \approx C_0$ [Eq. (17)]. Hence, the dielectric constant has to be evaluated from this regime as discussed before.

C. Effects of illumination intensity and AC frequency on capacitance-voltage measurement

The Lorentz dielectric function can accommodate all the effects of AC frequency, illumination and DC bias on the measured capacitance of M-S-M devices. To further confirm this, C-V measurements are performed on ITO/ZnO/PTB7/MoO_3/Ag device under dark and light conditions [Fig. 5(a)]. Because of the photogeneration, the peak position is shifted towards low voltage and the peak value increases. The increase in capacitance under illumination can be attributed to the increase in density of dipoles ($N \to N + \Delta N$), and the peak shift towards low voltage corresponds to the reductions in resonant frequency ($\omega_{0,\mathrm{Dark}} \to \omega_{0,\mathrm{Light}}$) and effective field inside the semiconductor. The simulated C-V curves of dark and light conditions are consistent with the experimental observation [Fig. 5(b)]. To address the effect of frequency, C-V measurements are performed on

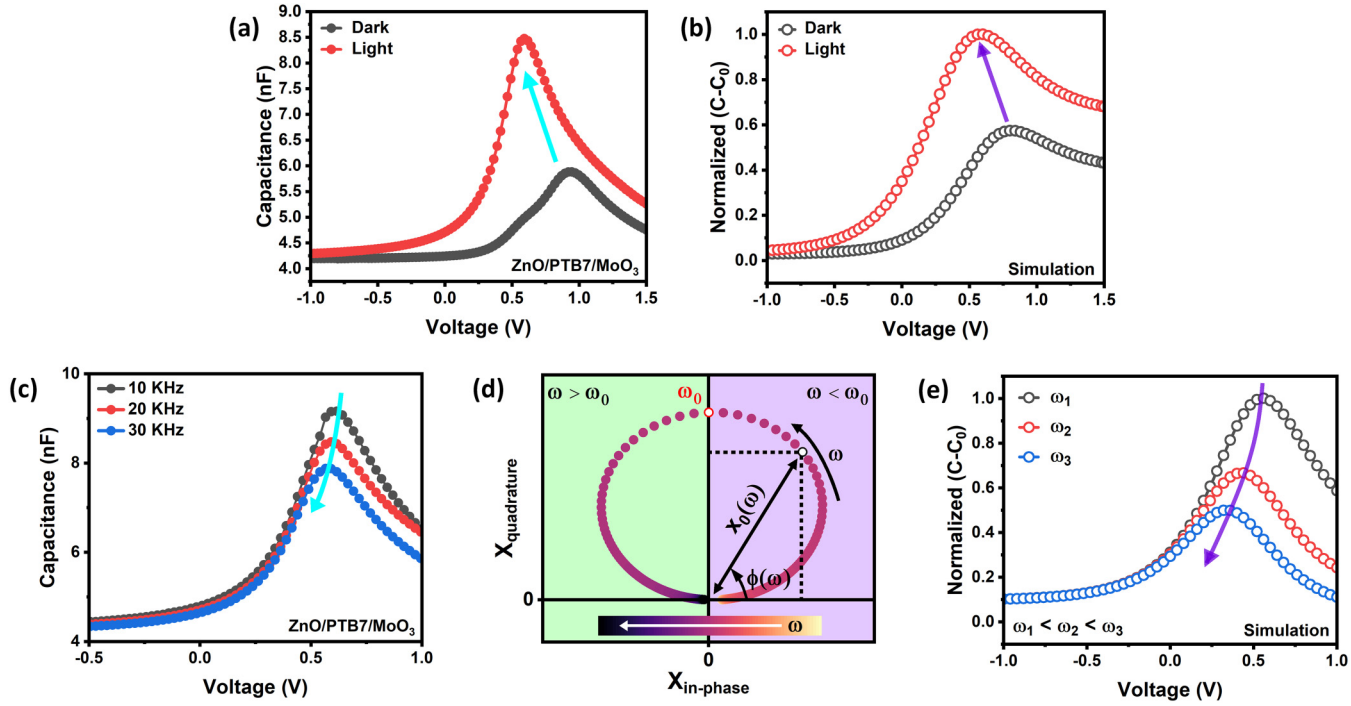

FIG. 5. (a) and (b) are the measured and simulated C-V curves under dark and light conditions, respectively. (c) The C-V curves measured at different AC frequencies. (d) The change in the in-phase ($x_{\text{in-phase}}$) and quadrature ($x_{\text{quadrature}}$) components of charge oscillations at different AC frequencies and (e) the simulations of C-V curves at different AC frequencies. All the measurements are done on ITO/ZnO/PTB7/MoO_3/Ag device.

ITO/ZnO/PTB7/MoO_3/Ag device at different AC frequencies as shown in Fig. 5(c). With the increase in measurement frequency, the peak value of capacitance decreases and the peak position is shifted towards the low voltage. If the measurement frequency is far from the resonance frequency, the in-phase component of charge oscillation ($x_{\text{in-phase}}$) is more and the quadrature component of charge oscillation ($x_{\text{quadrature}}$) is less [Fig. 5(d)]. The $x_{\text{in-phase}}$ component leads to the real part of the Lorentz dielectric function and is responsible for the energy storage (or capacitance). Whereas, the $x_{\text{quadrature}}$ component leads to the imaginary part of the Lorentz dielectric function and is responsible for the energy dissipation (see Sec. S2 in the Supplemental Material for more details) [63]. Hence, one can consider ϵ_r as a function of $(\omega_0^2 - \omega^2)$ rather than considering it as a function of ω alone. The simulations of C-V at different measurement frequencies are done on the basis of the above understanding and the results are shown in Fig. 5(e). The simulation results are consistent with the experimental observations further confirming the validity of the proposed theory and model.

IV. CONCLUSIONS

In conclusion, the Lorentz oscillator model of dielectric constant has been validated for M-S-M devices. The density of dipoles and the effective resonant frequency (ω_0) of the system are found to be changing with illumination intensity and DC bias. A novel technique, equilibrium photo-capacitance measurement (EPCM), has been used for probing ω_0 under different conditions of DC bias and illumination by measuring the equilibrium frequency (ω_e). A new model has been proposed to correlate ω_0 to the ratio of densities of free and bound carriers (N_f/N_b). The simulation results are consistent with the experimental data, confirming the validity of the model. Apart from this, the EPCM technique has been demonstrated as a tool for distinguishing the regions in C-V data where the effects of bound carriers, free carriers and background dielectric constant are dominant. Additionally, this technique has been used for finding the background dielectric constant of a material which is challenging to ascertain due to its sensitivity to measurement conditions.

ACKNOWLEDGMENTS

M.R.A. acknowledges the University Grants Commission (UGC), India for financial support. The authors acknowledge Professor Dieter Neher and Professor Joy Mitra for fruitful discussions. The authors acknowledge financial support from Science and Engineering Research Board (SERB) (Grant No. CRG/2021/003874) funded by the Department of Science and Technology (Government of India) and Indian Institute of Science Education and Research Thiruvananthapuram (IISER-TVM), Kerala, India.

DATA AVAILABILITY

The data that support the findings of this article are not publicly available. The data are available from the authors upon reasonable request.

[1] H. Ding, J. J. Liou, C. R. Cirba, and K. Green, An improved junction capacitance model for junction field-effect transistors, Solid-State Electron. **50**, 1395 (2006).

[2] A. Boukredimi, New capacitance–voltage model for linearly graded junction, J. Comput. Electron. **13**, 477 (2014).

[3] J. Kuk and S. Lee, Gate voltage-dependence of junction capacitance in MOSFETs, IEEE Trans. Electron. Devices **68**, 5315 (2021).

[4] J. W. Zhang, Y. He, X. Q. Chen, Y. Pei, H. M. Yu, J. J. Qin, and X. Y. Hou, Study on the basic capacitance–voltage characteristics of organic molecular semiconductors, Org. Electron. **21**, 73 (2015).

[5] J. V. Li, A. T. Neal, T. J. Asel, Y. Kim, and S. Mou, Effect of defects in capacitance-voltage measurement of doping profiles in Ga_2O_3, Thin Solid Films **782**, 140028 (2023).

[6] J. Mingu and W. Choi, Capacitance–voltage analysis of Al_2O_3/WS_2 metal-oxide-semiconductor capacitors, J. Phys. D **54**, 41LT01 (2021).

[7] C. Frisk, Y. Ren, J. Olsson, T. Törndahl, F. Annoni, and C. Platzer-Björkman, On the extraction of doping concentration from capacitance–voltage: A Cu2ZnSnS4 and ZnS sandwich structure, IEEE J. Photovoltaics **7**, 1421 (2017).

[8] A. Vais, J. Franco, K. Martens, D. Lin, S. Sioncke, V. Putcha, L. Nyns, J. Maes, Q. Xie, M. Givens, F. Tang, X. Jiang, A. Mocuta, N. Collaert, A. Thean, and K. De Meyer, A new quality metric for III–V/high-k MOS gate stacks based on the frequency dispersion of accumulation capacitance and the CET, IEEE Electron Device Lett. **38**, 318 (2017).

[9] Y. K. Lee, Study of charges in fluorinated polyimide film by using capacitance-voltage method, Mod. Phys. Lett. B **20**, 379 (2006).

[10] J. Schmidt, F. Rutz, V. Daumer, and R. Rehm, Capacitance-voltage investigation of low residual carrier density in InAs/GaSb superlattice infrared detectors, Infrared Phys. Technol. **84**, 3 (2017).

[11] H. Fujiwara and M. Kondo, Effects of carrier concentration on the dielectric function of ZnO: Ga and In_2 O_3: Sn studied by spectroscopic ellipsometry: Analysis of free-carrier and band-edge absorption, Phys. Rev. B **71**, 075109 (2005).

[12] X. Guo, M. Wang, and Z. Han, A frequency-dependent capacitance–voltage model for thin-film transistors, IEEE Trans. Electron. Devices **63**, 1666 (2016).

[13] A. M. Sonnet, C. L. Hinkle, D. Heh, G. Bersuker, and E. M. Vogel, Impact of semiconductor and interface-state capacitance on metal/high-k/GaAs capacitance–voltage characteristics, IEEE Trans. Electron. Devices **57**, 2599 (2010).

[14] I. Matacena, P. Guerriero, L. Lancellotti, E. Bobeico, N. Lisi, R. Chierchia, P. D. Veneri, and S. Daliento, Capacitance–voltage investigation of encapsulated graphene/silicon solar cells, IEEE Trans. Electron. Devices **70**, 4243 (2023).

[15] E. Itoh and M. Iwamoto, Interfacial electrostatic phenomena and capacitance–voltage characteristics of ultrathin polyimide Langmuir–Blodgett films, Elect. Eng. Jpn. **134**, 9 (2001).

[16] J. Ackaert, Z. Wang, E. De Backer, P. Colson, and P. Coppens, Non contact surface potential measurements for charging reduction during manufacturing of metal-insulator-metal capacitors, Microelectron. Reliability **41**, 1403 (2001).

[17] N. Preissler, J. A. Töfflinger, O. Gabriel, P. Sonntag, D. Amkreutz, B. Stannowski, B. Rech, and R. Schlatmann, Passivation at the interface between liquid-phase crystallized silicon and silicon oxynitride in thin film solar cells, Prog. Photovoltaics **25**, 515 (2017).

[18] H. Xie, Y. Sanchez, P. Tang, M. Espíndola-Rodríguez, M. Guc, L. Calvo-Barrio, S. López-Marino, Y. Liu, J. R. Morante, A. Cabot, *et al.*, Enhanced hetero-junction quality and performance of kesterite solar cells by aluminum hydroxide nanolayers and efficiency limitation revealed by atomic-resolution scanning transmission electron microscopy, Solar RRL **3**, 1800279 (2019).

[19] D. Menossi, E. Artegiani, A. Salavei, S. Di Mare, and A. Romeo, Study of $MgCl_2$ activation treatment on the defects of CdTe solar cells by capacitance-voltage, drive level capacitance profiling and admittance spectroscopy techniques, Thin Solid Films **633**, 97 (2017).

[20] Y. Kim and I.-H. Choi, Defect characterization in co-evaporated $Cu_2ZnSnSe_4$ thin film solar cell, Current Appl. Phys. **16**, 944 (2016).

[21] D. C. Tripathi, K. S. Rao, and Y. N. Mohapatra, Impact of defect states on the capacitance voltage characteristics of space charge limited organic diodes, and determination of defect states, J. Mater. Chem. C **9**, 4903 (2021).

[22] Q. Min, E.-P. Li, and J.-M. Jin, Modeling and analysis for MOS capacitance of TSV considering temperature dependence, in *2019 Joint International Symposium on Electromagnetic Compatibility, Sapporo and Asia-Pacific International Symposium on Electromagnetic Compatibility* (EMC Sapporo/APEMC) (IEEE, Sapporo, Japan, 2019), pp 350–353.

[23] A. Jüngel, R. Pinnau, and E. Röhrig, Analysis of a bipolar energy-transport model for a metal-oxide-semiconductor diode, J. Math. Anal. Appl. **378**, 764 (2011).

[24] E. Yu, S. Cho, and B.-G. Park, An accurate simulation study on capacitance-voltage characteristics of metal-oxide-semiconductor field-effect transistors in novel structures, Phys. B: Condens. Matter **521**, 305 (2017).

[25] M. Matsumura and Y. Hirose, Extraction of the capacitance of a metal oxide semiconductor tunnel diode (MOSTD) biased in accumulation, Jpn. J. Appl. Phys. **38**, L845, L845 (1999).

[26] A. S. Babadi, E. Lind, and L.-E. Wernersson, Modeling of n-InAs metal oxide semiconductor capacitors with high-κ gate dielectric, J. Appl. Phys. **116**, 214508 (2014).

[27] A. F. Basile and P. M. Mooney, Modeling of high-frequency capacitance-voltage characteristics to quantify trap distributions near SiO_2/SiC interfaces, J. Appl. Phys. **111**, 094509 (2012).

[28] B. Wang, H.-M. Zhang, H.-Y. Hu, B. Shu, Y.-M. Zhang, and J.-J. Song, High-frequency capacitance–voltage characteristics of N-type metal–oxide–semiconductor capacitor based on strained-Si/SiGe architecture, Jpn. J. Appl. Phys. **52**, 064201 (2013).

[29] S. B. Iyer, V. Kumar, and K. S. Harshavardhan, High-frequency capacitance-voltage characteristics of amorphous (undoped)/crystalline silicon heterostructures, Solid-State Electron. **34**, 535 (1991).

[30] J. Victory, C. C. McAndrew, and K. Gullapalli, A time-dependent, surface potential based compact model for MOS capacitors, IEEE Electron. Device Lett. **22**, 245 (2001).

[31] J. G. Petrov, E. E. Polymeropoulos, and H. Möhwald, Three-capacitor model for surface potential of insoluble monolayers, J. Phys. Chem. **100**, 9860 (1996).

[32] P. K. Manda, L. Karunakaran, S. Thirumala, A. Chakravorty, and S. Dutta, Modeling of organic metal–insulator–

semiconductor capacitor, IEEE Trans. Electron Devices **66**, 3967 (2019).
[33] A. Kumar and S. Rai, Compact modeling and analysis of charge and device capacitance for SELBOX junctionless transistor, Silicon **14**, 2565 (2022).
[34] O. Moldovan, B. Iñiguez, D. Jiménez, and J. Roig, Analytical charge and capacitance models of undoped cylindrical surrounding-gate MOSFETs, IEEE Trans. Electron Devices **54**, 162 (2006).
[35] A. Zhang, L. Zhang, Z. Tang, X. Cheng, Y. Wang, K. J. Chen, and M. Chan, Analytical modeling of capacitances for GaN HEMTs, including parasitic components, IEEE Trans. Electron. Devices **61**, 755 (2014).
[36] J. Dobeš, Reliable CAD analyses of CMOS radio frequency and microwave circuits using smoothed gate capacitance models, AEU Int. J. Electron. Commun. **57**, 372 (2003).
[37] C. Ucurum and H. Goebel, Quasi-static capacitance–voltage characteristics of pentacene-based metal–oxide–semiconductor structures, Microelectron. J. **44**, 606 (2013).
[38] S. Lee, Y. W. Jeon, S. Kim, D. Kong, D. H. Kim, and D. M. Kim, Comparative study of quasi-static and normal capacitance–voltage characteristics in amorphous indium-gallium-zinc-oxide thin film transistors, Solid-State Electron. **56**, 95 (2011).
[39] K. Takechi, M. Nakata, H. Kanoh, S. Otsuki, and S. Kaneko, Quasi-static capacitance–voltage characteristics of polycrystalline silicon thin-film transistors, Jpn. J. Appl. Phys. **45**, 6905 (2006).
[40] D. Boukredimi and H. Allouche, Accurate quasi static capacitance for abrupt homojunction under forward and reverse polarization, Bull. Mater. Sci. **36**, 251 (2013).
[41] C. P. Watson, M. Devynck, and D. M. Taylor, Photon-assisted capacitance–voltage study of organic metal–insulator–semiconductor capacitors, Org. Electron. **14**, 1728 (2013).
[42] G. I. Zebrev, A. A. Tselykovskiy, D. K. Batmanova, and E. V. Melnik, Small-signal capacitance and current parameter modeling in large-scale high-frequency graphene field-effect transistors, IEEE Trans. Electron. Devices **60**, 1799 (2013).
[43] R. B. Hallgren and P. H. Litzenberg, TOM3 capacitance model: Linking large-and small-signal MESFET models in SPICE, IEEE Trans. Microwave Theory Tech. **47**, 556 (1999).
[44] H. Eslahi, T. J. Hamilton, and S. Khandelwal, Small signal model and analog performance analysis of negative capacitance FETs, Solid-State Electron. **186**, 108161 (2021).
[45] J. Furlan, I. Skubic, F. Smole, P. Popović, and M. Topič, Small-signal capacitance and conductance of biased *a*-Si structures, J. Appl. Phys. **80**, 3854 (1996).
[46] M. Wiatr, P. Seegebrecht, and H. Peters, Charge based modeling of the inner fringing capacitance of SOI-MOSFETs, Solid-State Electron. **45**, 585 (2001).
[47] J. Zhang, J. He, X.-Y. Zhou, L.-N. Zhang, Y.-T. Ma, Q. Chen, X.-K. Zhang, Z. Yang, R.-F. Wang, Y. Han, *et al.*, A unified charge-based model for SOI MOSFETs applicable from intrinsic to heavily doped channel, Chin. Phys. B **21**, 047303 (2012).
[48] S. Khandelwal, F. M. Yigletu, B. Iniguez, and T. A. Fjeldly, A charge-based capacitance model for AlgGaAs/GaAs HEMTs, Solid-State Electron. **82**, 38 (2013).
[49] B. Yang, R. Huang, X. Zhang, and Y. Y. Wang, A charge-based intrinsic capacitance model for thin-film SOI short-channel MOSFET, Chin. J. Electron. **9**, 25 (2000).
[50] J. Ahmad, M. Sabir, M. Q. Awan, S. Anwar, M. E. Mazhar, R. A. Khalil, and S. H. Bukhari, Effect of Co_2 substitution on $MgAl_2O_4$ studied by infrared reflectance spectroscopy, Optik **147**, 180 (2017).
[51] B. Akaoglu, I. Atilgan, and B. Katircioglu, Thickness and optical constant distributions of PECVD a-SiCx: H thin films along electrode radial direction, Thin Solid Films **437**, 257 (2003).
[52] A. Dutta, V. Tiainen, H. A. Qureshi, L. Duarte, and J. J. Toppari, Modeling optical constants from the absorption of organic thin films using a modified Lorentz oscillator model, Opt. Mater. Express **12**, 2855 (2022).
[53] S. Saha, A. Dutta, C. DeVault, B. T. Diroll, R. D. Schaller, Z. Kudyshev, X. Xu, A. Kildishev, V. M. Shalaev, and A. Boltasseva, Extraordinarily large permittivity modulation in zinc oxide for dynamic nanophotonics, Mater. Today **43**, 27 (2021).
[54] S. Yu, T. Zhang, J. Dai, and K. Xu, Hybrid inverse design scheme for nanophotonic devices based on encoder-aided unsupervised and supervised learning, Opt. Express **31**, 39852 (2023).
[55] H. Singh, S. Kumar, and P. K. Sharma, Tunable exciton-plasmon coupled resonances with Cu_2/Cu substitution in self-assembled CuS nanostructured films, Appl. Surf. Sci. **612**, 155831 (2023).
[56] A. M. Schimpf, N. Thakkar, C. E. Gunthardt, D. J. Masiello, and D. R. Gamelin, Charge-tunable quantum plasmons in colloidal semiconductor nanocrystals, ACS Nano **8**, 1065 (2014).
[57] Z. Xu, X. Cui, S. Liu, and X. Yin, Excitation of surface plasmons with a long oscillation lifetime using silicon nanophotonic devices: A strong coupling system, Appl. Phys. Express **11**, 114002 (2018).
[58] W. Pan-Pan, Z. Yu-Zhi, P. Ming-Dong, Z. Yun-Long, W. Ling-Nan, C. Yun-Zhen, and S. Li-Xin, Spectroscopic ellipsometry analysis of vanadium oxide film in Vis-NIR and NIR-MIR, Acta Phys. Sin. **65**, 127201 (2016).
[59] S. G. Choi, L. M. Gedvilas, S. Y. Hwang, T. J. Kim, Y. D. Kim, J. Zúñiga-Pérez, and V. Muñoz Sanjosé, Temperature-dependent optical properties of epitaxial CdO thin films determined by spectroscopic ellipsometry and Raman scattering, J. Appl. Phys. **113**, 183515 (2013).
[60] E Márquez, E. Blanco, M. García-Gurrea, M. C. Puerta, M. D. de la Vega, M. Ballester, J. M. Mánuel, M. I. Rodríguez-Tapiador, and S. M. Fernández, Optical properties of reactive RF magnetron sputtered polycrystalline Cu_3N thin films determined by UV/Visible/NIR spectroscopic ellipsometry: An eco-friendly solar light absorber, Coatings **13**, 1148 (2023).
[61] H. A. Lorentz, *The Theory of Electrons and its Applications to the Phenomena of Light and Radiant Heat* (GE Stechert Company, New York, NY, 1916), Vol. 29.
[62] G. Grüner, *Electrodynamics of Solids: Optical Properties of Electrons in Matter* (Cambridge University Press, Cambridge, UK, 2002).
[63] See Supplemental Material at http://link.aps.org/supplemental/10.1103/y879-hx9f for more details about the experimental methods, and discussions about the microscopic origins of capacitance and photo-capacitance response, which also includes Refs. [64,65].

[64] A. Djurišić and E. Li, Modeling the index of refraction of insulating solids with a modified lorentz oscillator model, Appl. Opt. **37**, 5291 (1998).

[65] P. A. Kawka and R. O. Buckius, Optical properties of polyimide films in the infrared, Int. J. Thermophys. **22**, 517 (2001).

[66] M. Mohan, V. Nandal, S. Paramadam, K. P. Reddy, S. Ramkumar, S. Agarwal, C. S. Gopinath, P. R. Nair, and M. A. G. Namboothiry, Efficient organic photovoltaics with improved charge extraction and high short-circuit current, J. Phys. Chem. C **121**, 5523 (2017).

[67] R. A. Muhammed, A. Alexander, A. B. Pillai, V. K. Pulikodan, A. Joseph, and M. A. G. Namboothiry, Sequential photoluminescence measurements to explore electron-trapping dynamics in slow photoresponse materials: Zinc Oxide thin films as a model system, Phys. Rev. Appl. **19**, 064034 (2023).

[68] M. Chu, S.-B. Liu, A.-R. Yu, H.-M. Yu, J.-J. Qin, R.-C. Yi, Y. Pei, C.-Q. Zhu, G.-R. Zhu, Q.-Z., and X.-Y. Hou, Accurate capacitance–voltage characterization of organic thin films with current injection*, Chin. Phys. B **30**, 087301 (2021).

[69] H. E. Omari, A. Zyane, A. Belfkira, M. Taourirte, François Brouillette, Dielectric properties of paper made from pulps loaded with ferroelectric particles, J. Nanomater. (2016).

[70] V. M. Radivojević, S. Rupčić, M. Srnović, and G. Benšić, Measuring the dielectric constant of paper using a parallel plate capacitor, IJECES **9**, 1 (2018).

[71] A. Note, Solutions for measuring permittivity and permeability with LCR meters and impedance analyzers, Agilent Literature **1**, 25 (2008).

[72] K. S. Kim, R. K. Gupta, G. S. Chung, and F. Yakuphanoglu, Effects of illumination on capacitance characteristics of Au/3C-SiC/*p*-Si/Al diode, J. Alloys Compd. **509**, 10007 (2011).

[73] P. Chakrabarti, B. R. Abraham, A. Das, B. S. Sharan, and V. Maheshwari, Effect of illumination on the capacitance of a proposed MIS diode, Phys. Status Solidi A **128**, 513 (1991).

[74] A. Guerrero, J. Bisquert, and G. Garcia-Belmonte, Impedance spectroscopy of metal halide perovskite solar cells from the perspective of equivalent circuits, Chem. Rev. **121**, 14430 (2021).

[75] O. Almora, C. Aranda, E. Mas-Marzá, and G. Garcia-Belmonte, On Mott-Schottky analysis interpretation of capacitance measurements in organometal perovskite solar cells, Appl. Phys. Lett. **109**, 173903 (2016).

[76] C. Berthod, H. Zhang, A. F. Morpurgo, and T. Giamarchi, Theory of cross quantum capacitance, Phys. Rev. Res. **3**, 043036 (2021).

[77] G. Garcia-Belmonte, P. P. Boix, J. Bisquert, M. Sessolo, and H. J. Bolink, Simultaneous determination of carrier lifetime and electron density-of-states in P3HT:PCBM organic solar cells under illumination by impedance spectroscopy, Sol. Energy Mater. Sol. Cells **94**, 366 (2010).

[78] M. Mingebach, C. Deibel, and V. Dyakonov, Built-in potential and validity of the Mott-Schottky analysis in organic bulk heterojunction solar cells, Phys. Rev. B **84**, 153201 (2011).

[79] I. Mora-Seró, G. Garcia-Belmonte, P. P. Boix, M. A. Vázquez, and J. Bisquert, Impedance spectroscopy characterisation of highly efficient silicon solar cells under different light illumination intensities, Energy Environ. Sci. **2**, 678 (2009).

[80] J. Yuan, S. Yao, and P. Poulin, *Dielectric Constant of Polymer Composites and the Routes to High-k or Low-k Nanocomposite Materials* (Springer, Cham, Switzerland, 2016).

[81] M. P. Hughes, K. D. Rosenthal, N. A. Ran, M. Seifrid, G. C. Bazan, and T.-Q. Nguyen, Determining the dielectric constants of organic photovoltaic materials using impedance spectroscopy, Adv. Funct. Mater. **28**, 1801542 (2018).

[82] I. Constantinou, X. Yi, N. T. Shewmon, E. D. Klump, C. Peng, S. Garakyaraghi, C. K. Lo, J. R. Reynolds, F. N. Castellano, and F. So, Effect of polymer–fullerene interaction on the dielectric properties of the blend, Adv. Energy Mater. **7**, 1601947 (2017).